fluids

MDPI

Article

Structures of Ethanol Spray Flames under CO_2 Dilution of the Oxidizer in the Counterflow Configuration under MILD Combustion Conditions

Oscar Noreña and Eva Gutheil *

Interdisciplinary Center for Scientific Computing, Heidelberg University, 69120 Heidelberg, Germany; eva.gutheil@iwr.uni-heidelberg.de

* Correspondence: gutheil@iwr.uni-heidelberg.de

Received: 13 October 2020; Accepted: 27 October 2020; Published: 30 October 2020

Abstract: Structures of both gaseous and liquid ethanol flames in different oxidizing gas environments in the axisymmetric counterflow configuration at atmospheric pressure are studied. Initially, ethanol/air gas flames are considered where pure ethanol is directed against air at initial temperatures of 400 K, and N_2 is successively removed to obtain structures of ethanol/O_2 gas flames. Furthermore, the addition of CO_2 to the oxidizer side is carried out. Then, an ethanol spray is carried by air and directed against an air stream, and the same procedure is performed as described for the gas flames. The gas strain rate at the fuel side of the configuration is increased from low values of 55/s up to extinction, and the initial droplet diameter is varied. For the combustion of gaseous ethanol in air and in pure oxygen, the nitrogen removal results in an increase in the maximum flame temperature from 2010 K to 2920 K at a gas strain rate of 55/s on the fuel side of the configuration, and the extinction strain rates are 630/s and 26,000/s, respectively. It is confirmed that ethanol spray flames in air show two reaction zones at low strain whereas the lean ethanol spray flames in pure oxygen exhibit a single reaction zone in all situations studied. For increased liquid fuel mass flow rate to a global equivalence ratio of unity, two reaction zones are retrieved. An analysis regarding the addition of CO_2 in both the ethanol/oxygen gas and spray flames is also discussed and is found that CO_2 dilution of the carrier gas the spray is much more efficient than diluting the opposed gas stream in the counterflow configuration for the generation of MILD combustion conditions in oxy-fuel flames.

Keywords: MILD combustion; Ethanol-O_2 flames; CO_2 dilution

1. Introduction

Emissions of CO_2 as well as NO_X and soot during the combustion in power generation processes must be reduced to comply with stricter legal regulations. The consumption of energy is expected to increase by 37% within the next decades [1], which requires the development of new combustion technologies in order to simultaneously satisfy environmental and energy demands.

Recently, oxy-fuel combustion came into the focus of research. In this technology, either pure O_2 or a mixture of O_2 and recirculated flue gases are used as oxidizer, producing exhaust gases that mainly consist of a mixture of CO_2 and H_2O from which the water may be removed in order to capture the CO_2, which has a particularly high concentration in the oxy-fuel combustion products. A carbon capture and storage (CCS) strategy involving oxy-fuel combustion aims to reduce pollutant emissions as well as the volume of the flue gas [2]. Nevertheless, combustion instabilities, leakage of air into the flue gas system, and a relatively low energy efficiency [2] still constitute unresolved challenges to the technical realization of oxy-fuel combustion.

Another promising combustion technology, the moderate or intense low oxygen dilution (MILD), is characterized by a uniform temperature distribution, increased net radiation flux, low NOx emissions,

and very stable operating conditions [3–6]. MILD combustion is characterized by a strong recirculation of hot exhaust gases to preheat and dilute the reactive mixture. As a result, both a more uniform distribution and a lower rise of temperature inside the combustion chamber will occur, leading to an invisible flame front, a higher thermal efficiency, and lower concentrations of both NO_X and soot in the exhaust gases compared to conventional combustion systems [4]. The possibility to combine oxy-fuel combustion with the advantages of the MILD regime seems to be a promising approach for the aforementioned difficulties.

The combination of oxy-fuel and the MILD combustion strategies has already been the subject of both experimental and computational studies of combustion devices of laboratory scale. Negligible formation of soot, acetylene, and NO_X were measured in the flameless combustion of propane and oxygen compared to a conventional setup [7]. MILD oxy-combustion of coal was found to be stable during experiments conducted in air or in an Ar-O_2 mixture as oxidizers, where a burner with high exhaust-gas recirculation ratios [8] was used. The participation of CO_2 in chemical reactions during oxy-fuel combustion of methane was found to have a significant impact on the consumption and production rates of CO within a flameless combustor [9]. The influence of the initial CO_2 concentration, fuel-jet momentum rate, and equivalence ratio on the setting and stability of MILD oxy-fuel combustion was investigated for three different gaseous fuels [10]. While there is also research available regarding MILD combustion of liquid fuels [11–13], no studies on MILD oxy-fuel combustion of sprays are found. The factors affecting the stabilization and optimization of spray MILD oxy-fuel combustion will be investigated in the present study. The fuel ethanol is considered because it acts as addition to conventional fuels.

A present numerical analysis of the combustion characteristics using detailed chemistry is conducted in an axisymmetric counterflow configuration using an in-house computer code that was originally developed for the study of conventional spray flames [14,15]. At a first stage, subsequent replacement of N_2 by O_2 from the opposed gas stream of the fuel is conducted in an ethanol/air gas flame to obtain an ethanol/oxygen gas flame. Progressive addition of CO_2 to the oxidizer side is carried out to address the effect of O_2 dilution with CO_2, since it has been found that high concentrations of CO_2 in the reactive mixture affect the flame stability [2]. The same procedure is followed for an ethanol spray flame in air, where the spray is carried by air and directed against an air stream. The strain rate at the fuel side of the configuration is increased up to extinction, and the initial droplet diameter is varied for the mono-disperse spray. The structure of the reaction zones in spray counterflow flames at low strain [16,17] are studied for ethanol/air and ethanol/O_2 flames. Extinction of these spray flame structures is analyzed to study the differences between conventional, MILD, and MILD oxy-fuel combustion with respect to flame stability.

2. Mathematical Model

An Eulerian-Lagrangian description of a dilute spray flame in the counterflow configuration is considered [14,15]. The spray is assumed to be initially mono-disperse and equations accounting for the droplet heating, evaporation, and motion are solved. At elevated strain rates, the spray reverses and may oscillate leading to local polydispersity. An axisymmetric two-dimensional formulation is used for the gas phase, and after non-dimensionalization, a similarity analysis is applied to transform the governing equations into a one-dimensional system [14,17]. This transformation allows for the consideration of detailed chemical reaction schemes [15,17] for the oxidation of ethanol comprising 38 species and 337 elementary reactions [18]. The chemical reaction scheme was validated [19] with respect to flame speed and ignition delay times and represents a high-temperature chemical reaction scheme with no nitrogen chemistry.

2.1. Governing Equations

For the gas phase, the general conservation equations of mass, momentum, mass fractions of chemical species, and energy under consideration of spray source terms accounting for the interaction of the gas and the spray are written as [15]

$$\frac{\partial \rho}{\partial t} + \frac{\partial \left(\rho u_i\right)}{\partial x_i} = S_\mathrm{v} \tag{1}$$

$$\rho \frac{\partial u_j}{\partial t} + \rho u_j \frac{\partial}{\partial x_i} = -\frac{\partial p}{\partial x_j} - \frac{\partial \tau_{ij}}{\partial x_i} - u_j S_\mathrm{v} + S_\mathrm{m,j} \tag{2}$$

$$\rho \frac{\partial Y_k}{\partial t} + \rho u_i \frac{Y_k}{\partial x_i} + \frac{\partial}{\partial x_i}\left(\rho V_{k,i} Y_k\right) = \dot{\omega}_k + \left(\delta_{Fk} - Y_k\right) S_\mathrm{v}, \;\; k = 1, \ldots, N \tag{3}$$

$$\begin{aligned} \rho C_p \frac{\partial T}{\partial t} + \rho u_i C_p \frac{\partial T}{\partial x_i} = &- \sum_{k=1}^{N} h_k \dot{\omega}_k + \frac{\partial p}{\partial t} + u_i \frac{\partial p}{\partial x_i} + \frac{\partial}{\partial x_i}\left(\lambda \frac{\partial T}{\partial x_i}\right) - \rho \frac{\partial T}{\partial x_i} \sum_{k=1}^{N} C_{p,k} Y_k V_{k,i} \\ &- \tau_{i,j} \frac{\partial u_i}{\partial x_j} - S_\mathrm{v} \int_{T_0}^{T} C_{p,F} dT + S_\mathrm{e}, \end{aligned} \tag{4}$$

where u_i is the gas velocity in i direction, ρ is the gas density, Y_k denotes the mass fraction of species k, C_p and $C_{p,k}$ are the specific heat capacities at constant pressure for the mixture and the species k, respectively, p is the static pressure, h_k is the enthalpy of species k, and λ stands for the heat conductivity. S_v, $\mathbf{S}_\mathrm{m}$, and S_e are the mass, momentum, and energy source terms accounting for the interaction between the gas and liquid phases, $V_{i,k}$ is the diffusion velocity, V_k, of species k in i direction within the mixture. δ denotes the Kronecker symbol, the subscript F represents the fuel, and $\dot{\omega}_k$ describes the specific chemical reaction rate for the species k, $k = 1, ..., N$. The diffusion coefficient of species k in the mixture is D_k, and D_T is the thermal diffusion coefficient. The viscous stress tensor τ_{ij} is defined by

$$\tau_{ij} = -\mu\left(\frac{\partial u_i}{\partial x_j} + \frac{\partial u_j}{\partial x_i}\right) + \frac{2}{3}\mu \frac{\partial u_k}{\partial x_k}\delta_{ij}, \tag{5}$$

where μ is the dynamic gas viscosity.

The physical properties are calculated following the work of Kee et al. [20]. In particular, the multicomponent diffusion model is used in the present study.

2.2. Liquid Phase

For the liquid fuel spray, a discrete droplet model is used that considers each droplet group represented by a single droplet for every axial position. Even though mono-disperse sprays are considered in the study, the occurrence of droplet reversal and oscillation cause local poly-dispersity. Thus, for each droplet size group k, the corresponding equation is formulated. The equation for the droplet motion can be written as

$$m_k \frac{d\mathbf{v}_k}{dt} = \pi R_k^2 \frac{1}{2} \rho_\mathrm{l} \left(\mathbf{u} - \mathbf{v}_k\right) \left|\mathbf{u} - \mathbf{v}_k\right| C_{\mathrm{D},k} + m_k \mathbf{g}, \tag{6}$$

where $k = 1, ..., K$, and K is the total number of different droplet size classes. $C_{\mathrm{D},k}$ is the drag coefficient, $\mathbf{v}_k$ and $\mathbf{u}$ stand for the droplet and gas velocity, respectively, R_k is the droplet radius of size group k, $m_{k=\frac{4}{3}\pi R_k^3 \rho_\mathrm{l}}$ is the mass of a droplet with radius R_k, and ρ_l denotes the liquid density. The droplet evaporation rate $\dot{m}_k$ of a droplet of size group k is described by the Abramzon-Sirignano model [21]

$$\dot{m}_k = 2\pi R_k \rho_{\mathrm{f},k} D_{\mathrm{f},k} \widetilde{\mathrm{Sh}}_k \ln\left(1 + \mathrm{B}_{\mathrm{M},k}\right). \tag{7}$$

Here, the subscript f stands for properties in the film surrounding the droplets. $\widetilde{\mathrm{Sh}}_k$ is the modified Sherwood number to account for convective droplet evaporation, and $B_{\mathrm{m},k}$ is the Spalding mass transfer number

$$B_{\mathrm{m},k} = \left(Y_{\mathrm{F_s},k} - Y_{\mathrm{F}}\right) / \left(1 - Y_{\mathrm{F_s},k}\right) \tag{8}$$

where Y_{F} is the mass fraction of the fuel vapor, and $Y_{\mathrm{F_s},k}$ denotes the fuel mass fraction at the droplet surface given by

$$Y_{\mathrm{F_s},k} = \frac{M_{\mathrm{F}} X_{\mathrm{F_s},k}}{M_{\mathrm{F}} X_{\mathrm{F_s},k} + \left(1 - X_{\mathrm{F_s},k}\right) \overline{M}}. \tag{9}$$

$\overline{M}$ denotes the mean molecular weight of the gas and $X_{\mathrm{F_s},k}$ is the mole fraction of the fuel F at the surface s of the droplets

$$X_{\mathrm{F_s},k} = \frac{p_{\mathrm{v}}}{p}, \tag{10}$$

where p_{v} is the vapor pressure at the droplet surface.

For droplet heating, the diffusion-limit model

$$\frac{\partial T_{\mathrm{l},k}}{\partial t} = \alpha_{\mathrm{l}} \frac{1}{r^2} \frac{\partial}{\partial r} \left(r^2 \frac{\partial T_{\mathrm{l},k}}{\partial r} \right) \tag{11}$$

is used, where $T_{\mathrm{l},k}$ is the temperature of the liquid and r the radial coordinate inside the droplet. Radiative and convective heat transfer inside the droplet are neglected since heat conduction is the dominant process for the conditions under investigation. Droplet interaction is neglected for the dilute spray under consideration. Thus, the droplet number density, n_k of droplet size group k yields

$$\frac{\partial n_k}{\partial t} + \frac{\partial \left(n_k v_{i,k}\right)}{\partial x_i} = S_{n,k}. \tag{12}$$

$S_{n,k}$ denotes the source term accounting for changes in the droplet number density due to droplet reversal or oscillation [15]. Additionally, the source terms for mass, momentum, and energy appearing in Equations (1) to (4) are written as

$$S_{\mathrm{v}} = \sum_{k=1}^{K} n_k \dot{m}_k \tag{13}$$

$$\mathbf{S}_{\mathrm{m}} = \sum_{k=1}^{K} \left[- n_k m_k \frac{d\mathbf{v}_k}{dt} + n_k \dot{m}_k \mathbf{v}_k \right] \tag{14}$$

$$S_{\mathrm{e}} = \sum_{k=1}^{K} \left[- n_k [\dot{q}_k + \dot{m}_k L_{\mathrm{v}}(T_{\mathrm{l},k})] + n_k \dot{m}_k \int_{T_0}^{T_{s,k}} C_{p,F} dT \right], \tag{15}$$

which includes the energy transferred to the droplet,

$$\dot{q}_k = \dot{m}_k [C_{p,F}(T - T_{s,k}) / B_{T,k} - L_{\mathrm{v}}(T_{l,k})], \tag{16}$$

where $B_{T,k}$ is the Spalding heat transfer number, and L_{v} the temperature-dependent latent heat of vaporization.

Boundary and initial conditions are provided in the next section, where the liquid or gaseous fuel side of the configuration is denoted by the subscript $-\infty$ and the opposed gas side by ∞. The coupled equations for the gas and the liquid phases are solved numerically using a hybrid scheme [14,15,17].

3. Results and Discussion

Both structures of ethanol gas and spray flames in different gaseous oxidizing environments are presented and discussed.

3.1. Gas Flames

Figure 1 (left) displays an ethanol/air gas flame at low strain rate, where ethanol at atmospheric pressure is directed against an air stream of the same temperature. The initial gas temperature of 400 K is well above the boiling temperature of ethanol at atmospheric pressure. Then the progressive replacement of N_2 by O_2 is carried out to obtain an ethanol/O_2 flame, cf. Figure 1 (right). Please note that the axial position 0 mm identifies the gas stagnation plane. The maximum gas temperature of the ethanol/air flame is 2010 K, and the flame resides on the oxidizer side of the configuration, which is typical for these flames [15,17]. The peak value of the CO mass fraction near 0.8 mm is closer to the fuel side of the configuration than the maximum flame temperature, since CO is produced prior to CO_2 and the carbon-containing fuel enters from the left side of the configuration. CO_2 attains a peak at about 1.6 mm since CO_2 is mainly produced through the reaction

$$\mathrm{CO} + \mathrm{OH} \rightleftharpoons \mathrm{CO_2} + \mathrm{H}. \tag{17}$$

The width of the chemical reaction zone is about 4.8 mm.

The right part of Figure 1 displays the structure of the ethanol/O_2 gas flame at the corresponding conditions. The removal of nitrogen causes an increase of the maximum flame temperature to 2920 K since nitrogen acts as a damping factor to the chemical reactions in the ethanol/air flame. As a consequence, the mass fractions of the products in the ethanol/oxygen flame are considerably higher compared to the combustion in air, and the chemical reaction zone broadens to about 7.3 mm, which is also associated with the preferential diffusion of oxygen. The peak of the CO mass fraction of 0.48 is located at an axial position of about −0.64 mm, i.e., it resides on the fuel side of the configuration, whereas the CO_2 mass fraction peaks at 0.83 mm on the oxidizer side of the configuration due to the widening of the chemical reaction zone. The flame temperature still attains its maximum at the oxidizer side of the flame.

In view of the addition of CO_2 to the system, the reaction rate of the chemical reaction CO + OH ⇌ CO_2 + H is analyzed and shown in Figure 2. The net molar chemical reaction rate for CO_2 and the corresponding production and consumption rates, the gas temperature, and the mole fractions of the chemical species involved in the above chemical reaction are plotted against the axial position for the ethanol/air (left) and the ethanol/O_2 (right) gas flames. In the pure oxygen flame, more CO is produced on the fuel side of the flame, which may reverse the direction of the above chemical reaction, leading to decomposition of CO_2. Once the temperature reaches a value of 2500 K, the direction of the chemical reaction reverses again since it is endothermic, and CO_2 is produced in the hot part of the flame. Towards the gas side of the configuration, the chemical reaction rate decreases until a temperature of 1500 K is reached, at the edge of the chemical reaction zone at an axial position of about 4 mm. The concentrations of the H and OH radicals are about 10 times higher in the ethanol/O_2 flame compared to the ethanol/air flame.

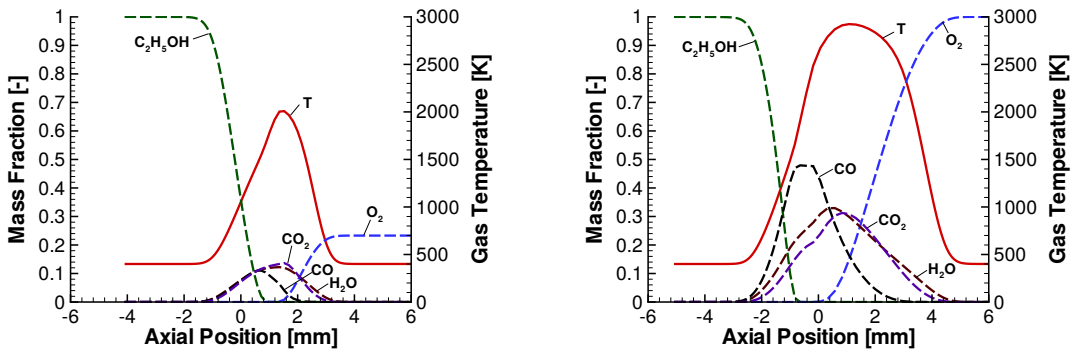

Figure 1. Structures of ethanol/air (**left**) and ethanol/O_2 (**right**) gas flames at inlet temperatures of 400 K and a gas strain rate of $a_{-\infty} = 55/\mathrm{s}$ on the fuel side of the configuration.

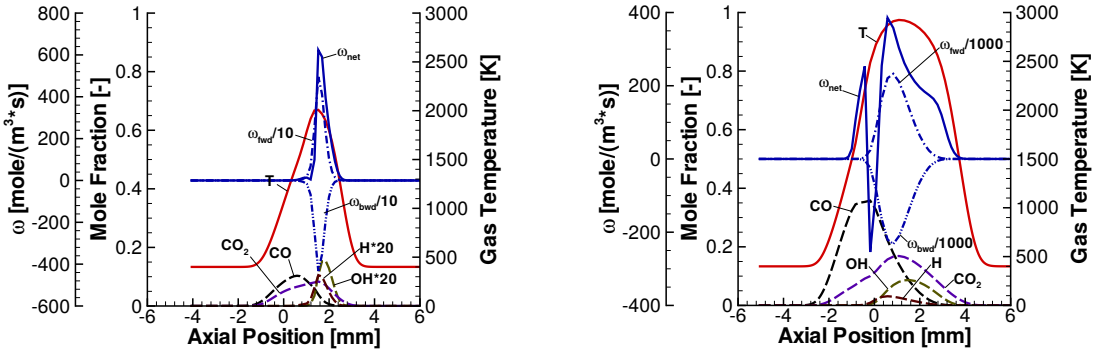

Figure 2. Analysis of the reaction rate CO + OH ⇌ CO_2 + H of ethanol/air (**left**) and ethanol/O_2 (**right**) gas flames for the conditions of Figure 1.

In a next step, dilution of O_2 with 0.67 mass fraction of CO_2 on the oxidizer side of the flame is conducted, and the chemical reaction rates of production and consumption of CO_2 observed under this condition are compared to that of the undiluted flame. All other conditions are kept constant.

When the oxidizer side of the gaseous ethanol/O_2 flame is diluted with CO_2, both the structure of the flame and the reaction rates of the chemical reaction CO_2 + H → CO + OH change. The left part of Figure 3 shows that CO_2 dilution causes a strong decrease in the peak flame temperature from 2900 K to 2217 K compared to the pure ethanol/oxygen gas flame. This has been explained [22] to be mainly related to the reaction CO_2 + H → CO + OH, which is the reverse reaction of the main CO to CO_2 oxidation step in most combustion systems [23]. The consumption of the hydrogen atoms retards the main chain-branching reaction H + O_2 → H + OH, affecting the structure and chemical composition of the inner flame structure [24].

The right part of Figure 3 shows how the direction of the chemical reaction CO + OH ⇌ CO_2 + H changes throughout the chemical reaction zone. On the fuel side of the configuration, where initial CO_2 production was found in both the ethanol/air and the undiluted ethanol/oxygen flame, the relatively high concentration of CO_2 prevents this in the present CO_2-diluted flame. The peak of CO occurs at an axial position of 0.5 mm, and it is produced until the chemical consumption rate of CO reaches its peak of −1300 moles/(m^{3}s) at 0.97 mm. It is also noticed that an increase in the slope of CO_2 mass fraction exists at that location, which is high enough to reverse its reaction with OH, which enables an increase of the CO_2 mass fraction to 520 moles/(m^{3}s) at 1.45 mm. The chemical reaction zone for this diluted oxy-flame has a width of 5.6 mm, which represents a decrease of 17% in comparison with the non-diluted oxy-flame.

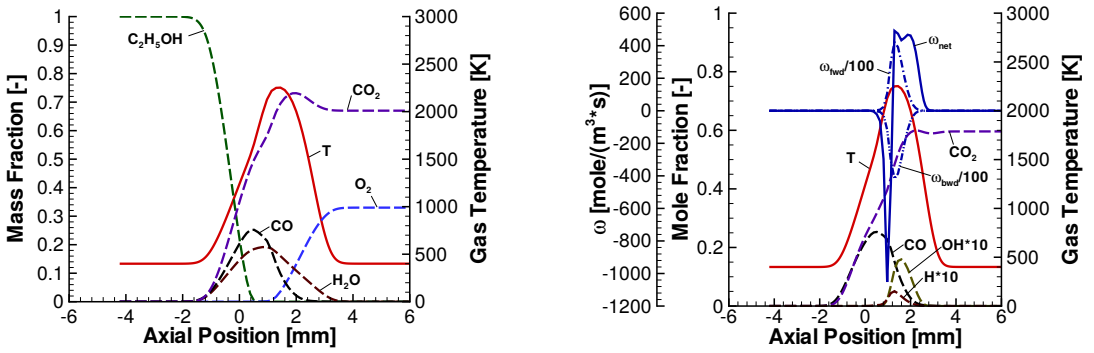

Figure 3. Outer flame structure (**left**) and analysis of the chemical reaction rate CO + OH ⇌ CO_2 + H (**right**) for an ethanol/O_2-CO_2 gas flame for the conditions of Figure 1 with $Y_{CO_2,\infty} = 0.67$.

3.2. Spray Flames

Furthermore, an ethanol/air spray flame is subjected to an analogous procedure. In all spray flame simulations, the initial gas and liquid temperatures are 300 K at atmospheric pressure, i.e., the ethanol is liquid as it enters the configuration. Mono-disperse sprays with different initial droplet sizes are studied, and the structures and maximum flame temperature are determined. Moreover, the chemical production and consumption rates of CO_2 under undiluted and diluted conditions are discussed. Gas strain rates at the spray side of the configuration from 55/s up to extinction for the different droplet sizes ares studied, and the effect of this parameter on the reversal point of the droplet as well as its reentrance to the reaction zone are discussed. The effects of the global equivalence ratio E on the structure of the spray flame and on the maximum temperature of the flame will be shown.

In the counterflow configuration where the ethanol spray is introduced from the left side of the configuration, oxygen may enter from either side of the configuration, i.e., it may act as carrier gas for the spray and/or it may be directed against the spray flow. Previous computations [14,15,17] assumed the equivalence ratio of the spray side of the configuration, $E_{-\infty}$ to be unity. This definition does not take into account the possible effect of different gases and oxygen amounts in the gas flow that is directed against the spray. Therefore, the definition in the present paper is extended to a global definition of the equivalence ratio E, to account for this.

The expression for the equivalence ratio calculated at the spray side of the configuration $E_{-\infty}$ may be written as [14,15]

$$E_{-\infty} = \left(\frac{\nu_{ox}}{\nu_F}\right)_{st} \left(\frac{M_{O_2}}{M_F}\right) \frac{m_{spray}}{\rho_{-\infty} Y_{O_2 -\infty}}, \tag{18}$$

where m_{spray} denotes the total volumetric initial spray mass. Thus, for a given initial spray mass, the equivalence ratio can be computed or the equivalence ratio is chosen and the initial volumetric liquid mass may be computed, which is the procedure pursued in the present paper.

If the opposed gas stream is pure O_2 or diluted with CO_2, the definition of the global equivalence ratio, E, taking the oxygen-containing species coming from the opposed spray side of the configuration, must be modified to account for this. In the present definition, the spray and the gas velocities of the carrier gas are assumed to be identical since this is a condition for the similarity transformation to hold [14,15], and it is denoted by $u_{-\infty}$. Considering the initial mass flow rates of either sides of the counterflow configuration, the global equivalence ratio may be written as

$$E = \left(\frac{\nu_{ox}}{\nu_F}\right)_{st} \left(\frac{M_{O_2}}{M_F}\right) \frac{u_{-\infty} m_{spray}}{\rho_{-\infty} u_{-\infty} Y_{O_2 -\infty} + \rho_{\infty} u_{\infty} \left[Y_{O_2 \infty} + Y_{CO_2 \infty}\, \mu_{O_2, CO_2}\right]}, \tag{19}$$

where a mixture of oxygen and nitrogen carries the spray, and $Y_{O_2 -\infty}$ denotes the mass fraction of oxygen in that mixture. The μ_{O_2, CO_2} denotes the mass fraction of O_2 in CO_2. The gas velocity of the opposed gas stream may be obtained as [14]

$$u_{\infty} = -a_{\infty} y_{\infty} = -\sqrt{\frac{\rho_{-\infty}}{\rho_{\infty}}}\, a_{-\infty} y_{\infty}, \tag{20}$$

or it results from the numerical simulation for given initial gas velocity and gas strain rate at the spray boundary of the configuration. ν_F and ν_{ox} are the stoichiometric coefficients of the global chemical reaction, M denotes the molecular weight of the species, and y is the physical coordinate, and the index st denotes stoichiometric conditions. The subscripts $-\infty$ and ∞ denote the boundaries at the fuel and the opposed sides of the configuration, respectively.

According to the previous equations and depending on the considered equivalence ratio, the initial droplet number density can be calculated from the initial total spray mass m_{spray} and the mass of a single droplet of radius R_0 as

$$n_{-\infty} = \frac{m_{spray}}{4/3 \pi R_0^3 \rho_l}, \tag{21}$$

where ρ_l denotes the liquid density.

First, calculations are performed with an equivalence ratio $E_{-\infty} = 1$.

The ethanol-air/air spray counterflow flame shown in the left part of Figure 4 was studied earlier [17]. Characteristics of this flame are the two reaction zones on the spray and on the gas side of the configuration with the mono-disperse spray completely evaporating just before reaching the stagnation plane where the flame temperature shows a local minimum. The maximum flame temperatures in both the reaction zones is about 2050 K.

The right part of Figure 4 shows the same spray flame where the nitrogen coming from the gas side of the configuration is replaced by oxygen to produce an ethanol spray in air directed against oxygen. The temperature of the spray-sided peak is slightly higher than that of the gas side, 2070 K and 2059 K, respectively. The profiles of the chemical species show also two peaks except for CO which reaches a single peak of 0.12 at a position of -1.4 mm. It is also at this position where the lowest temperature of 1754 K between the two peaks occurs. The maximum mass fraction of CO_2 is 0.15 and locates at an axial position of 0.4 mm, while its smaller peak of 0.14 is located at -3.8 mm. For H_2O, the highest mass fraction is located at -1.3 mm and has a value of 0.16. The width of the chemical reaction zone is 9.2 mm and the droplets do not reach the stagnation plane before they evaporate completely at an axial position of -0.93 mm.

The structure of the spray-sided flame remains largely unaffected of the replacement of nitrogen by oxygen on the gas side of the configuration whereas the reaction zone on the gas side shows a dramatical increase of flame temperature to 2660 K. This is accompanied by an elevation of the mass fractions of the reaction products such as CO_2 and H_2O. The width of the spray flame increases somewhat but not to the same extent as for the gas flames. This difference may be caused by the energy-consuming liquid fuel evaporation delaying the combustion in the gas phase.

In a next step, the carrier gas air of the spray is replaced by pure oxygen, and it is directed against pure oxygen, see left part of Figure 5 as well as against oxygen diluted gas by CO_2 with an initial mass fraction of 0.67, which is displayed on the right side of the same figure. The most challenging difference in these flame structures is that a single chemical reaction zone is obtained in both situations. The local minimum in the profile of gas temperature in case of the ethanol/air spray flames is attributed to the presence of major fuel spray evaporation which strongly consumes energy from the gas flame. For the highly reactive liquid ethanol spray flames in pure oxygen on both sides of the configuration or with somewhat CO_2-diluted flames on the gas side of the configuration, the spray evaporation is easily compensated by the heat of combustion in particular, since the spray evaporation occurs entirely on the spray side of the configuration. The carrier gas of the spray seems to have a greater influence on the spray flame structure than the gas stream that is directed against the spray. In fact, the dilution of the oxygen stream on the gas side of the counterflow configuration does not seem to have much influence at all, except of course for the different profiles of CO_2 on the RHS of the flame structures.

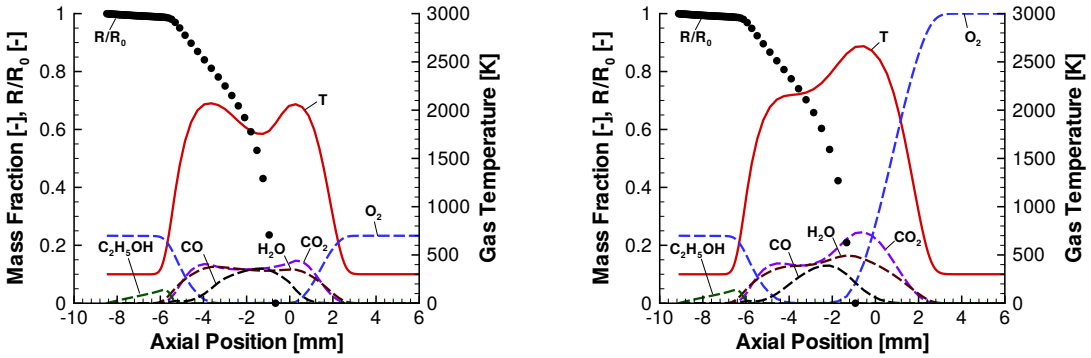

Figure 4. Structures of ethanol-air/air (**left**) [17] and ethanol-air/O_2 (**right**) spray flames, inlet temperatures of 300 K, $a_{-\infty} = 55/\text{s}$, $E_{-\infty} = 1$, and $R_0 = 25$ µm.

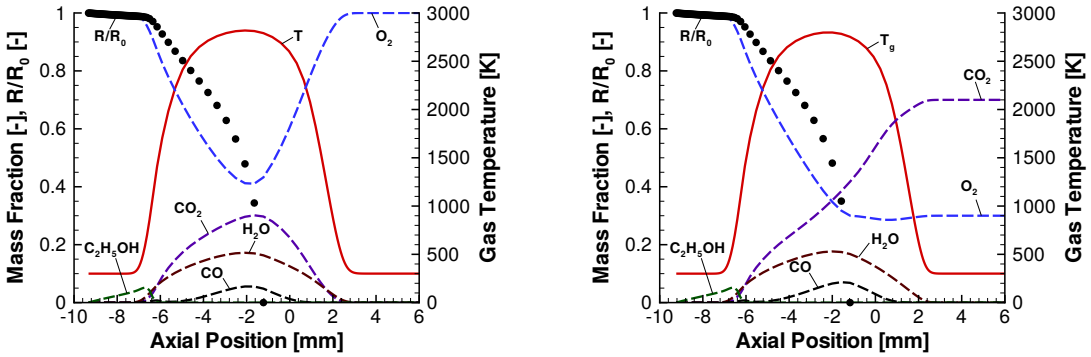

Figure 5. Structures of ethanol-O_2/O_2 (**left**) and ethanol-O_2/CO_2-O_2 (**right**) spray flames, inlet temperatures of 300 K, $a_{-\infty} = 55/\text{s}$, $E_{-\infty} = 1$, $R_0 = 25$ µm, $Y_{CO_2,\infty} = 0.67$, and $R_0 = 25$ µm.

The maximum flame temperatures of the flames in Figure 5 only differ by 20 K. The conclusion here is that the CO_2 addition does not influence the structure under the present conditions because the global equivalence ratio E, cf. Equation (19), of the spray flames is very lean, i.e., it is about 0.1 for the ethanol air flames and about 0.3 for the ethanol spray flames in oxygen or with CO_2 addition, whereas $E_{-\infty} = 1$. In the computations discussed so far, the spray-sided equivalence ratio was always set to unity, and the addition of oxygen and CO_2 to the system for fixed initial liquid mass modifies the global equivalence ratio E, see Equation (19) as discussed above. The successive removal of nitrogen by oxygen has made the spray flames so lean that the addition of CO_2 far away from the fuel side, where the interesting processes such as evaporation and combustion happen, does not affect the flame. The chemical reaction rate of the reaction CO + OH $\rightleftharpoons$ CO_2 + H for the different spray flames shown in Figures 6 and 7 confirm this.

Figures 6 and 7 display the chemical reaction rates of the chemical reaction CO + OH $\rightleftharpoons$ CO_2 + H, where forward, reverse, and net reaction rates are plotted for the four different flames that were presented so far. Please note that the net reaction rate for the spray flame with air in all streams attains chemical reaction rates of a factor 10 less that all others which reflects the damping character of the nitrogen in the air. The profiles of the net reaction rate shows a strong peak in the spray-sided reaction zone, this is the region where CO and OH have been produced and promote the forward reaction. A comparison of the two flames in Figure 7 without (left) and with(right) CO_2 dilution show that the peak of the reverse reaction, i.e., dissociation of CO_2 is enhanced and occurs somewhat further on the gas side of the configuration compared to the non-diluted flame, but the gas of this dissociation is compensated through a larger forward reaction, leading to similar net reaction rates for the pure oxygen compared to the CO_2-diluted flame. This explains the small differences found in the structures of these two flames.

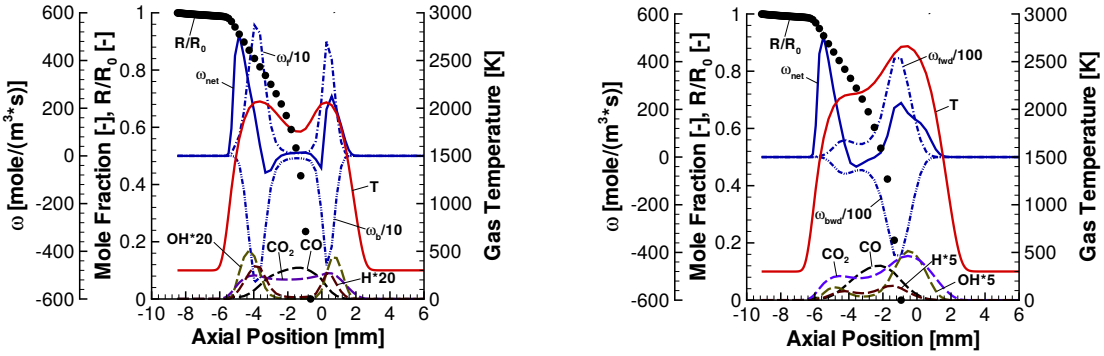

Figure 6. Ethanol-air/air (**left**) and ethanol-air/O_2 (**right**) spray flame temperature, chemical reaction rate of CO + OH $\rightleftharpoons$ CO_2 + H, mole fractions of participating chemical species, inlet temperatures of 300 K, $R_0 = 25$ µm, $a_{-\infty} = 55/\text{s}$.

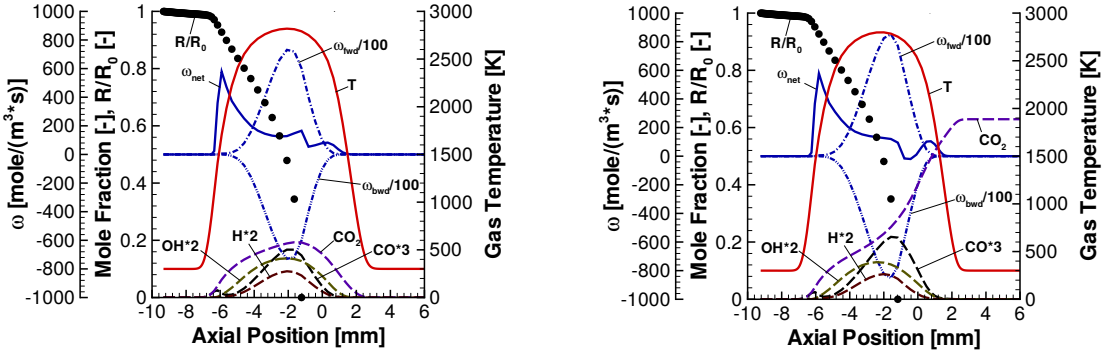

Figure 7. Ethanol-O_2/O_2 (**left**) and ethanol-O_2/CO_2-O_2 (**right**) spray flame temperature, chemical reaction rate of CO + OH $\rightleftharpoons$ CO_2 + H, $Y_{CO_{2,\infty}} = 0.67$ and mole fractions for inlet temperatures of 300 K, $R_0 = 25$ µm, $a_{-\infty} = 55/\text{s}$.

Moreover, the variation of both initial droplet size and gas strain rate on the spray side of the configuration, $a_{-\infty}$ is studied. These parameters were modified for different combinations of fuel sprays in air [15,17] or of liquid oxygen in gaseous hydrogen [25]. For all cases, $E_{-\infty} = 1$. In the following, initial droplet radii of 30, 40, and 50 µm are considered for gas strain rates of $a_{-\infty} = 55/\text{s}$ up to extinction.

Figure 8 displays the ethanol-O_2/O_2 spray flames at low (left) and high (right) strain rates just prior to extinction for an initial droplet radius of 40 µm. The flame structures for the other droplet radii are similar and therefore, they are not shown in detail. The maximum temperature decreases with increased strain rate, but the width of the flame is smaller for the case of larger droplets at low strain rate, while for high strain rates, the width of the flame is higher for larger droplets [15]. This is related to the higher inertia of larger droplets, which are able to cross the stagnation point and penetrate deeper into the flame, extending the chemical reaction zone.

A survey of all simulations for both gas (left) and spray (right) flames is provided in Figure 9. The maximum gas temperature is plotted against the gas strain rate on the fuel side, $a_{-\infty}$. Concerning the gas flames, the N_2 removal results in an increase in the maximum flame temperature from 2010 K to 2900 K with extinction strain rates of 630/s and 26,000/s for the flame burning in air and in O_2, respectively. The present results for ethanol combustion confirms the fact that combustion in oxygen is much more stable compared to that in air [26].

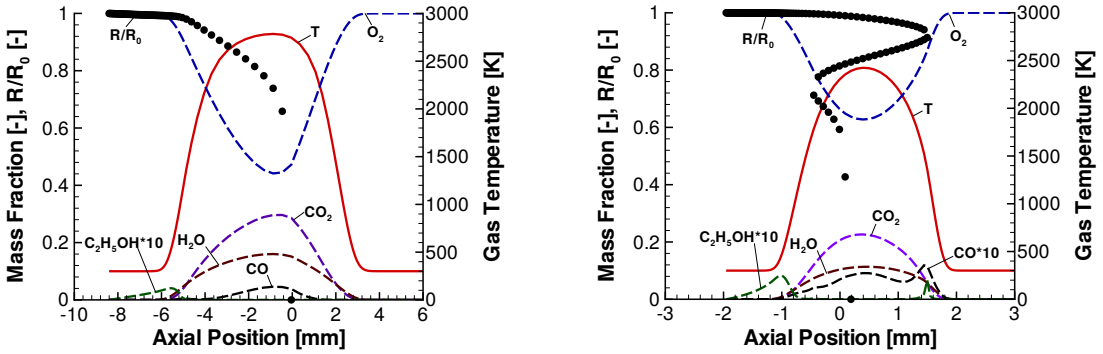

Figure 8. Structures of ethanol-O_2/O_2 spray flames for inlet temperatures of 300 K, $a_{-\infty} = 55/\text{s}$ (**left**) and $a_{-\infty} = 640/\text{s}$ (**right**), and $R_0 = 40$ µm.

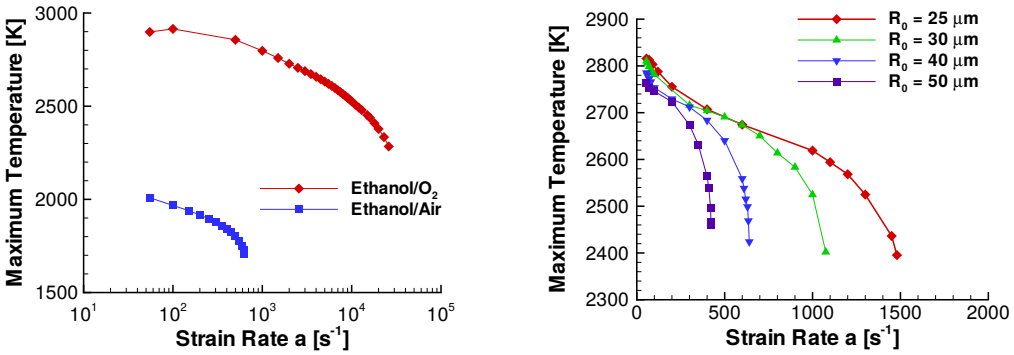

Figure 9. Maximum flame temperature versus fuel-sided gas strain rate for the ethanol/air and the ethanol/O_2 gas flames (**left**) and for ethanol-O_2/O_2 spray flames for initial droplet radii from 25 μm to 50 μm (**right**).

The right part of Figure 9 displays an analogous plot for the spray ethanol oxy-flame for different initial droplet sizes. The initial droplet radius of 25 μm shows the highest strain rate at extinction, namely 1490/s, and it decreases with an increase of the initial droplet radius with the lowest value of 425/s for an initial droplet radius of 50 μm. The extinction strain rate of the ethanol-O_2/O_2 spray flame can be compared to that of an ethanol-air/air spray flame [17] at the same conditions: the extinction strain rate of 1375/s is lower than that of the oxy-fuel spray flame of 1490/s. These results suggest a higher stability of ethanol spray combustion in oxygen compared to air.

Spray flames in air show two reaction zones in counterflow configuration at low strain [16,17]. At higher strain, these reaction zones merge and droplet reversal and oscillation may enhance combustion, which is associated with an increase of flame temperature with strain. This is not found in the present simulations of ethanol sprays in oxygen. The absence of the nitrogen enhances chemical reactions, and no local minimum of the flame temperature near the stagnation plane is found, so that in all situations studied here, a single chemical reaction zone is found. Both droplet reversal and oscillation are found in ethanol spray combustion in oxygen, but the enhancement of the chemical reactions that would lead to the above effect of increase of flame temperature with increased strain rate is not present, which may be due to the high chemical reactivity of oxy-combustion, where even more combustion efficiency through re-entry of the spray into the combustion zone may not be possible. An increase of initial droplet size leads to less stability of the spray flame, cf. Figure 9, which is in agreement with previous results for methanol spray combustion in air [15,16].

More simulations are performed to study the effect of CO_2 dilution of oxygen on the spray side instead of the gas side of the counterflow configuration. For this purpose, the carrier gas oxygen is diluted with CO_2 mass fractions of 0.4 and with 0.8. This leads to a decrease of the maximum temperature for the ethanol/O_2 flame (cf. the left part of Figure 5) from 2820 K to 2760 K for the diluted flame with a CO_2 mass fraction of 0.4 and to 2620 K for the 0.8 CO_2 mass fraction spray flame, see Figure 10 left and right parts, respectively. On the right part of Figure 10, a second chemical reaction zone develops on the spray side of the configuration at about −3.6 mm. For the spray flame where O_2 is diluted by a CO_2 mass fraction of 0.4, E is 0.22 and $E = 0.07$ for a CO_2 mass fraction of 0.8. Dilution of O_2 with CO_2 on the fuel side of the configuration for the ethanol-O_2/O_2 spray flame reduces also the overall equivalence ratio, but unlike in the case of dilution with CO_2 on the gas side of the configuration, a reduction of temperature is clearly visible for CO_2 dilution of the carrier gas. Thus, it is much more efficient to dilute the carrier gas with CO_2 than diluting the opposed gas stream in the counterflow configuration. Since $E_{-\infty}$ is fixed to unity for all cases, less liquid fuel is injected into the calculation domain if O_2 is diluted with CO_2 at the spray side, reducing in that way the initial volumetric liquid mass flow rate, which causes retardation of the chemical reactions and a reduced flame temperature.

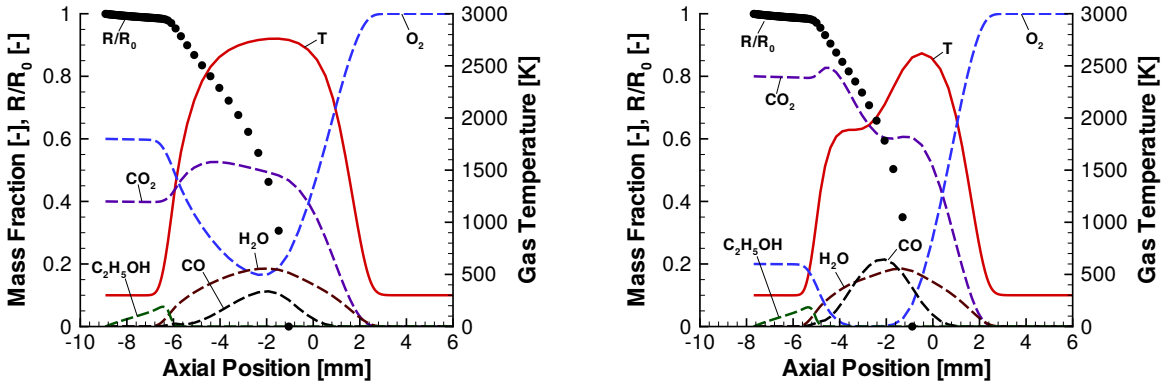

Figure 10. Ethanol-O_2-CO_2/O_2 spray flame structure for inlet temperatures of 300 K, $R_0 = 25$ µm, $Y_{CO_2,-\infty} = 0.4$ (**left**), $Y_{CO_2,-\infty} = 0.8$ (**right**), and $a_{-\infty} = 55/\text{s}$.

Figure 11 shows ethanol spray flames with the same conditions presented in Figure 4, but the global equivalence ratio E is set to unity, i.e., the liquid mass flow rate is increased, cf. Equations (18) and (19). Now all flame structures show two chemical reaction zones which are considerably broader than the flames with $E_{-\infty} = 1$. The flame width for the ethanol-air/air, ethanol-air/O_2, ethanol-O_2/O_2, and the ethanol-O_2/O_2-CO_2 flames for $E = 1$ are 12.0 mm, 18.4 mm, 44.0 mm, and 35.0 mm respectively. The corresponding values for Figures 4 and 5 are 9.5 mm, 10.0 mm, 11.0 mm, and 10.0 mm. This is a consequence of the higher liquid volume flux and the oxygen entering the configuration, leading to enhanced combustion and a broadening of the chemical reaction zone.

The maximum temperature for the ethanol-air/air flame shown in the left part of Figure 11 is 2060 K at an axial position of −6.1 mm, i.e., on the spray side of the configuration. Another the smaller temperature peak of 2040 K is located at 0.94 mm at the gas side of the counterflow configuration. The local minimum between the chemical reaction zones is 1310 K, which is considerably lower than that of the lower equivalence ratio. This reduced gas temperature is associated with the higher amount of liquid fuel, which requires more energy transfer from the gas phase for the evaporation process.

The replacement of air on the gas side of the configuration by oxygen is shown in the right part of Figure 11. This leads to an increase of gas temperature on the gas side of the configuration that reaches 2850 K. The spray-sided temperature peak is 1995 K, which is very similar to the flame with pure air. Moreover, the flame with oxygen instead of air at the gas side is considerably broader and product species mass fractions are increased as discussed above.

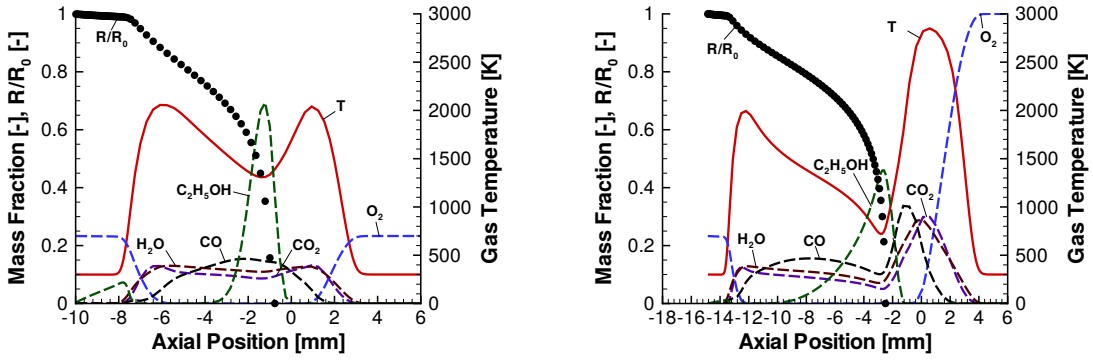

Figure 11. Ethanol-air/air and ethanol-air/O_2 spray flame structures for inlet temperatures of 300 K, $a_{-\infty} = 55/\text{s}$, $R_0 = 25$ µm, and $E = 1$.

Finally, ethanol spray flames carried by oxygen and directed against an oxygen stream with CO_2 dilution are shown in Figure 12, where the global equivalence ration is varied between 0.6 (left) and 0.8 (right). A stoichiometric flame sits at the spray nozzle, and an increase of the spray velocity and its

carrier gas is required to obtain a reasonable numerical solution. The increase of the global equivalence ratio from 0.6 to 0.8 does not significantly change the peak temperatures of the two chemical reaction zones which are about 3000 K for the spray-sided flame and about 2800 K on the gas side. An increase of the equivalence ratio E requires a higher initial volumetric liquid mass, and the evaporation regime is broadened leading to a wider spray flame by about 4 mm.

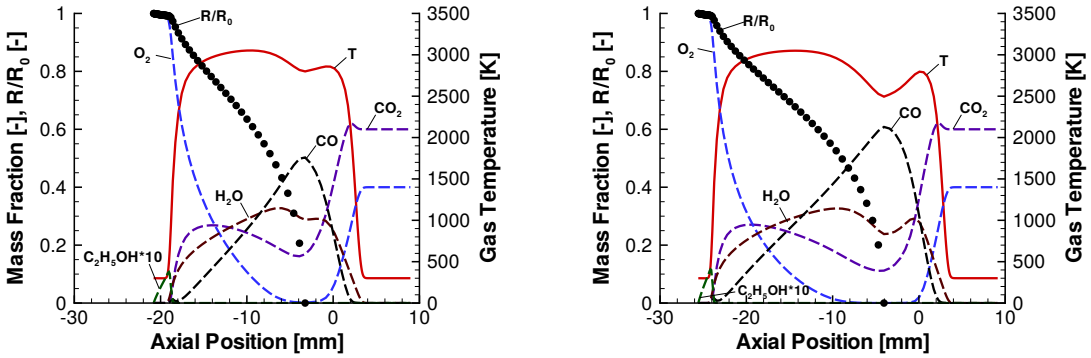

Figure 12. Ethanol-O_2/CO_2-O_2 spray flame structures for inlet temperatures of 300 K, $a_{-\infty} = 55/\mathrm{s}$, $R_0 = 25$ µm, $Y_{CO_2\infty} = 0.6$, and $E = 0.6$ (**left**) and $E = 0.8$ (**right**).

4. Summary and Conclusions

Structures of both gaseous and liquid ethanol flames are studied, where ethanol droplets are initially carried by an air stream flowing against air, are studied and subjected to an increase of the O_2 mass fraction while N_2 removal is conducted correspondingly, first on the gas side and then on the spray side of the configuration, until an oxy-fuel flame is obtained. In case of pure gas flames, the initial temperatures are 400 K, which is well above the boiling temperature of ethanol at atmospheric pressure, and for the spray flames, the initial temperatures are 300 K.

The structure of the oxy-fuel ethanol gas flame depicts a higher maximum temperature and a broader chemical reaction zone in comparison with that of the ethanol-air flame. Removal of N_2 and its replacement by O_2 enhances chemical reactions and causes the mass fraction profiles of the main chemical species to increase in comparison with that of ethanol-air flames. An analysis of the chemical reaction rate of CO + OH $\rightleftharpoons$ CO_2 + H, which is mainly responsible for the CO_2 formation, allows analyzing the participation of CO_2 in the chemical reactions. This chemical reaction reverses for a higher CO_2 dilution of the oxy-fuel flame, but it recovers beyond a temperature of about 2500 K due to its endothermic character. Further addition of CO_2 to the gas side of the configuration reduces the flame temperature, and the higher mass fraction of CO_2 may cause the suppression of the initial CO_2 production that is present at the beginning of the chemical reaction zone on the spray side of the configuration for the non-diluted combustion of ethanol in oxygen and in air. The reason for this peak in the CO_2 production rate at the fuel-rich side of the chemical reaction zone might be explained through the higher mass fraction of O_2 that is present in this region, but this needs further evaluation of the chemical reaction rates.

The successive increase of the initial droplet radius from 25 µm to 30 µm, 40 µm, and 50 µm, and the variation of the gas strain rate at the fuel side $a_{-\infty}$ from 55/s up to extinction are also carried out for both gas and spray oxy-fuel flames. The results confirm that oxy-fuel combustion is much more stable than conventional combustion in air. For spray combustion in air at stoichiometric conditions at the spray side of the configuration, an increase of the gas strain rate causes the two chemical reaction zones that exist at low strain rates to merge and at higher strain rates [15], and the maximum flame temperature increases due to droplet reversal and oscillation, leading to reentry into the chemical reaction zone. This is not observed in the case of the oxy-fuel spray flames at $E_{-\infty} = 1$ studied here since the already high chemical reactivity may not further be increased.

Ethanol spray flames with an overall equivalence ratio close to unity show considerably broader chemical reaction zones compared to the lean flames, and two chemical reaction zones are identified in contrast to the lean flames with a single chemical reaction zone. The higher liquid volume flux associated with the higher equivalence ratio as well as combustion of ethanol sprays in oxygen instead of air both lead to enhanced combustion and a broadening of the chemical reaction zone. The reasons for the broadening in these situations, however, is different: in the first situation, the increased liquid mass flow rate causes the evaporation zone to broaden whereas in the oxy-fuel combustion, the absence of the damping effect of nitrogen is responsible for the flame broadening.

Dilution of O_2 with CO_2 reduces the maximum temperature attained in the counterflow configuration for the gaseous oxy-fuel ethanol flames. For the ethanol oxy-fuel spray flames calculated with $E_{-\infty}$, a similar reduction of the maximum gas temperature is not observed if the CO_2 is added to the gas side of the counterflow configuration. When E is reduced from unity to 0.8 and 0.6 for the calculation of the ethanol spray oxy-fuel flames diluted by CO_2 on the gas side of the configuration, there is also no noticeable reduction of the maximum temperature. Dilution of O_2 by CO_2 in the gas stream of the counterflow configuration alone does not have a determinant effect to reduce maximum temperature in ethanol oxy-fuel spray flames as it is characteristic for MILD oxy-fuel combustion of gas combustion. Further increase of the gas strain for O_2-diluted flames should be conducted to find out if a decrease of the maximum attainable temperature is possible. However, a CO_2 dilution of the carrier gas of the spray leads to considerable reduction of the spray flame temperature in oxy-fuel spray combustion and is much more efficient in reducing the flame temperature and generating MILD combustion conditions than diluting the opposed gas stream in the counterflow configuration.

The high recirculation ratio of exhaust gases in MILD combustion also produces intense turbulence, which is closely related with high values of $a_{-\infty}$. The structures of these laminar spray flames may be used for implementation into a spray flamelet model for turbulent spray combustion [27,28].

Future studies will include higher alcohols including propanol and butanol.

Author Contributions: O.N. performed the numerical simulations, analyzed and plotted the results. E.G. contributed the original computer code, supervised the study, and revised the manuscript. All authors have read and agreed to the published version of the manuscript.

Funding: Oscar Noreña thanks Colciencias for the financial support through a research scholarship. The authors gratefully acknowledge the financial support of the German Research Foundation (DFG) through the Heidelberg Graduate School "HGS MathComp".

Conflicts of Interest: The authors declare no conflict of interest.

Nomenclature

a	gas strain rate on the spray side of the configuration [s^{-1}]
B_M	Spalding mass transfer number [-]
B_T	Spalding heat transfer number [-]
C_p	specific heat capacity at constant pressure [J kg^{-1} K^{-1}]
C_D	drag coefficient [-]
D	diffusion coefficient [kg m^{-2}]
E	global equivalence ratio [-]
$E_{-\infty}$	equivalence ratio at the fuel side of the configuration [-]
$\mathbf{g}$	gravitational acceleration [m s^{-2}]
h	specific enthalpy [J kg^{-1}]
k	index of chemical species [-]
K	number of droplet size classes [-]
L_v	temperature-dependent latent heat of vaporization [J kg^{-1}]
m	mass [kg]
$\dot{m}_k$	mass evaporation rate of a droplet of size class k [kg s^{-1}]

M	molecular weight [kg mol^{-1}]
n	droplet number density [m^{-3}]
N	total number of chemical species [-]
p	pressure [kg m^{-1} s^{-2}]
p_v	vapor pressure at the droplet surface [kg m^{-1} s^{-2}]
$\dot{q}_k$	heat transfer to droplet k [J s^{-1}]
r	radial coordinate inside a spherically symmetric droplet [m]
R	droplet radius [m]
S_e	energy source term [kg m^{-1} s^{-3}]
$\mathbf{S}_\mathrm{m}$	momentum source term [kg m^{-2} s^{-2}]
$S_{n,k}$	source term of droplet number density [m^{-3} s^{-1}]
S_v	mass source term [kg m^{-3} s^{-1}]
$\widetilde{\mathrm{Sh}}$	modified Sherwood number [-]
t	time [s]
T	gas temperature [K]
$T_\mathrm{l,k}$	temperature of droplets of size group k [K]
$\mathbf{u}$	gas velocity [m s^{-1}]
$\mathbf{v}$	droplet velocity [m s^{-1}]
$V_{k,i}$	diffusion velocity of species k in i direction [m s^{-1}]
$X_{\mathrm{F_s,k}}$	mole fraction of the Fuel F at the droplet surface s of species k [-]
$Y_{\mathrm{F_s,k}}$	mass fraction of the Fuel F at the droplet surface s of species k [-]
λ	thermal conductivity [kg m s^{-3} K^{-1}]
ν	stoichiometric coefficient [-]
ρ	gas density [kg m^{-3}]
ρ_l	liquid density [kg m^{-3}]
$\tau_{i,j}$	viscous stress tensor [kg m^{-1} s^{-2}]
$\dot{\omega}_k$	specific chemical reaction rate of species k [kg m^{-3} s^{-1}]
∞	boundary conditions at the gas side of the counterflow configuration
$-\infty$	boundary conditions at the spray side of the counterflow configuration

References

1. International Energy Agency (IEA). *World Energy Outlook*; IEA: Paris, France, 2020.
2. Chen, L.; Yong, S.Z.; Ghoniem, A.F. Oxy-fuel combustion of pulverized coal: Characterization, fundamentals, stabilization and CFD modeling. *Prog. Energy Combust. Sci.* **2012**, *38*, 156–214. [CrossRef]
3. Wünning, J.A.; Wünning, J.G. Flameless oxidation to reduce thermal NO-formation. *Prog. Energy Combust. Sci.* **1997**, *23*, 81–94. [CrossRef]
4. Cavaliere, A.; Joannon, M. Mild Combustion. *Prog. Energy Combust. Sci.* **2004**, *30*, 329–366. [CrossRef]
5. Si, J.; Wang, G.; Mi, J. Characterization of MILD Combustion of a Premixed CH4/Air Jet Flame versus Its Conventional Counterpart. *ACS Omega* **2019**, *4*, 22373–22384. [CrossRef] [PubMed]
6. Huang, X.; Tummers, M.J.; Roekaerts, D.J.E.M. Experimental and numerical study of MILD combustion in a lab-scale furnace. *Energy Procedia* **2017**, *120*, 395–402. [CrossRef]
7. Krishnamurti, N.; Paul, P.J.; Blasiak, W. Studies on low-intensity oxy-fuel burner. *Proc. Combust. Inst.* **2009**, *32*, 3139–3146. [CrossRef]
8. Stadler, H.; Ristic, D.; Förster, M.; Schuster, A.; Kneer, R.; Scheffknecht, G. NO_x-emissions from flameless coal combustion in air, Ar/O_2 and CO_2/O_2. *Proc. Combust. Inst.* **2009**, *32*, 3131–3138. [CrossRef]
9. Heil, P.; Toporov, D.; Förster, M.; Kneer, R. Experimental investigation on the effect of O_2 and CO_2 on burning rates during oxyfuel combustion of methane. *Proc. Combust. Inst.* **2011**, *33*, 3407–3413. [CrossRef]
10. Li, P.; Dally, B.; Mi, J.; Wang, F. MILD oxy-combustion of gaseous fuels in a laboratory-scale furnace. *Combust. Flame* **2013**, *160*, 933–946. [CrossRef]
11. Weber, R.; Smart, J.P.; vd Kamp, W. On the (MILD) combustion of gaseous, liquid, and solid fuels in high temperature preheated air. *Proc. Combust. Inst.* **2005**, *30*, 2623–2629. [CrossRef]

12. Reddy, V.M.; Trivedi, D.; Sawant, D.; Kumar, S. Investigations on Emission Characteristics of Liquid Fuels in a Swirl Combustor. *Combust. Sci. Technol.* **2015**, *187*, 469–488. [CrossRef]
13. Rodrigues, H.C.; Tummers, M.J.; van Veen, E.H.; Roekaerts, D.J.E.M. Spray flame structure in conventional and hot-diluted combustion regime. *Combust. Flame* **2015**, *162*, 759–773. [CrossRef]
14. Continillo, G.; Sirignano, W. Counterflow spray combustion modeling. *Combust. Flame* **1990**, *81*, 325–340. [CrossRef]
15. Gutheil, E.; Sirignano, W. Counterflow spray combustion modeling with detailed transport and detailed chemistry. *Combust. Flame* **1998**, *113*, 92–105. [CrossRef]
16. Gutheil, E. Multiple solutions for structures of laminar counterflow spray flames. *Prog. Comput. Fluid Dyn.* **2005**, *5*, 414–419. [CrossRef]
17. Gutheil, E. Structure and extinction of laminar ethanol/air spray flames. *Combust. Theor. Model.* **2001**, *5*, 131–145. [CrossRef]
18. Chevalier, C. Entwicklung eines detaillierten Reaktionsmechanismus zur Modellierung der Verbrennungsprozesse von Kohlenwasserstoffen bei Hoch- und Niedertemperaturbedingungen. Ph.D. Thesis, Universität Stuttgart, Stuttgart, Germany, 1993.
19. Warnatz, J.; Maas, U.; Dibble, R.B. *Combustion*; Springer: Heidelberg, Germany, 2006.
20. Kee, R.B.; Dixon-Lewis, G.; Warnatz, J.; Coltrin, M.E.; Miller, J.A.; Moffat, H.K. *A Fortran Computer Code Package for the Evaluation of Gas-Phase, Multicomponent Transport Properties*; Sandia Report SAND86-8246B; Sandia National Laboratories: Albuquerque, NM, USA, 1998.
21. Abramzon, B.; Sirignano, W. Droplet vaporization model for spray combustion calculations. *Int. J. Heat Mass Tran.* **1989**, *32*, 1605–1618. [CrossRef]
22. Liu, F.; Guo, H.; Smallwood, G.J.; Gülder, Ö.L. The chemical effects of carbon dioxide as an additive in an ethylene diffusion flame: Implications for soot and NO_x formation. *Combust. Flame* **2001**, *125*, 778–787. [CrossRef]
23. Westbrook, C.K.; Dryer, F.L. Chemical kinetic modeling of hydrocarbon combustion. *Prog. Energy Combust. Sci.* **1984**, *10*, 1–57. [CrossRef]
24. Normann, F.; Andersson, K.; Johnsson, F.; Leckner, B. Reburning in oxy-fuel combustion: A parametric study of the combustion chemistry. *Ind. Eng. Chem. Res.* **2010**, *49*, 9088–9094. [CrossRef]
25. Schlotz, D.; Gutheil, E. Modeling of Laminar Mono- and Bidisperse Liquid Oxygen/Hydrogen Spray Flames in the Counterflow Configuration. *Combust. Sci. Technol.* **2000**, *158*, 195–210. [CrossRef]
26. Urzica, D.; Gutheil, E. Structures of Laminar Methane/Nitrogen/Oxygen, Methane/Oxygen and Methane/Liquid Oxygen Counterflow Flames for Cryogenic Conditions and Elevated Pressures. *Z. Phys. Chem.* **2009**, *223*, 651–667. [CrossRef]
27. Hollman, C.; Gutheil, E. Flamelet-Modeling of Turbulent Spray Diffusion Flames Based on a Laminar Spray Flame Library. *Combust. Sci. Technol.* **1998**, *135*, 678–696. [CrossRef]
28. Hu, Y.; Kai, R.; Kurose, R.; Gutheil, E.; Olguin, H. Large eddy simulation of a partially pre-vaporized ethanol reacting spray using the multiphase DTF/flamelet model. *Int. J. Multiph. Flow* **2020**, *125*, 103216. [CrossRef]